IEEE Access
Multidisciplinary | Rapid Review | Open Access Journal

Received April 25, 2018, accepted May 18, 2018, date of publication May 30, 2018, date of current version July 19, 2018.

Digital Object Identifier 10.1109/ACCESS.2018.2842028

Large-Complex-Surface Defect Detection by Hybrid Gradient Threshold Segmentation and Image Registration

GUANGZHONG CAO[1], (Senior Member, IEEE), SONGBO RUAN[1], YEPING PENG[1], (Member, IEEE), SUDAN HUANG[1], (Member, IEEE), AND NGAIMING KWOK[2]

[1]Shenzhen Key Laboratory of Electromagnetic Control, College of Mechatronics and Control Engineering, Shenzhen University, Shenzhen 518060, China
[2]School of Mechanical and Manufacturing Engineering, University of New South Wales, Sydney, NSW 2052, Australia

Corresponding author: Yeping Peng (yeping.peng@szu.edu.cn)

This work was supported in part by the National Natural Science Foundation of China under Grant 51677120, in part by the Shenzhen Science and Technology Project, China, under Grant JCYJ20170818100522101, and in part by the Natural Science Foundation of Shenzhen University, China, under Grant 2017032.

ABSTRACT Machine vision-based object detection techniques have been widely used in product inspection, defect detection, and dimension measurement. These techniques have largely improved the efficiency of industrial production and increased the level of production autonomy. However, demands on advance hardware design and image processing algorithms are needed for the quality inspection of a large-complex-surface. In order to solve this problem, a hybrid surface defect detection method is developed. An image of the product surface is first divided into two areas: background with similar features and special pattern area, such as product trademarks. For the background area, defects have significant differences in gray intensity from the normal area. Fault detection is conducted using a gradient threshold segmentation method that can limit segmentation errors arising from uneven illuminations. For the special pattern area, image registration and image difference are adopted to detect defects, which are adaptive to irregular image contents with discontinuous shapes and appearances. Experimental results indicate that the proposed method achieves about 1.21 times and 2.94 times higher accuracy, in *F-measure*, for large-complex-surface defect detection than the traditional methods of gradient threshold segmentation and template matching, respectively. The proposed image processing technique can be applied in product quality inspections.

INDEX TERMS Large-complex-surface, defect detection, gradient threshold segmentation, image registration.

I. INTRODUCTION

Surface quality is one of the most crucial consideration of product appearance. Therefore, surface defect detection is an important process for product quality evaluation [1]. Machine vision based detection techniques have been widely used in agriculture product, metal sheet, consumer electronics surface inspection for its advantage as a straightforward, fast and low-cost approach; it also prompts the automation of product quality inspection [2]. Due to the influence of size, shape and detection environment, research should be conducted regarding different application requirements. However, only few reports are available on large-complex-surface product surface defect detection [3].

Existing surface visual perception methods mainly focus on small-scale objects, such as cell phone shells, fruits and optical elements and large-scale objects with simple surface shapes like metal sheets, leather and LCD panels [4], [5]. Surface defect detection for large-scale products requires high standard hardware including cameras and illumination sources for image collection and the image processing procedure is complicated. Therefore, methods making use of infrared [6]–[8], laser [9] and linear array camera scanning [10] are often used to obtain surface information of large-scale objects. However, scanning methods require the assistance from motion drives and their efficiencies are affected by the conveying speed. When the object has a large size and requires three-dimensional screening, traditional scanning methods are time-consuming and inefficient, which greatly limit their uses in practical applications. Therefore, using area-array camera for rapid surface image

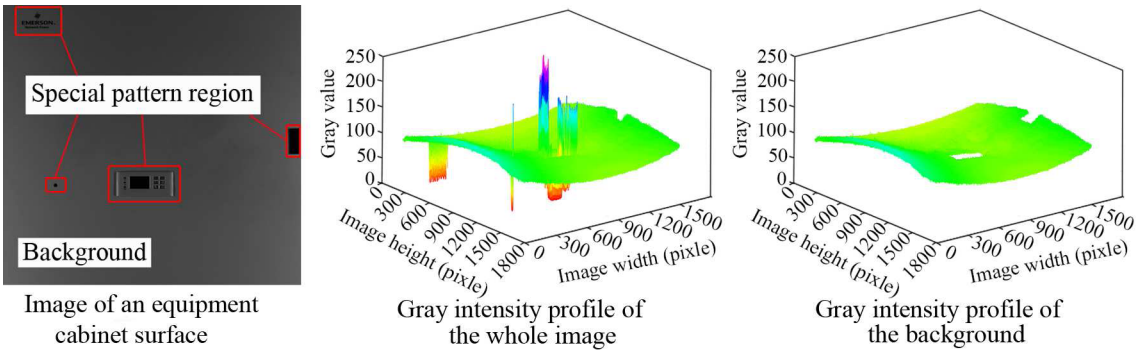

FIGURE 1. Equipment cabinet surface image and its gray intensity profile.

acquisition is becoming more and more popular in defect detection [11].

Image-based surface defect detection methods are composed of threshold segmentation [12], edge detection [13] and template matching [14]. When a defect exists on the product surface, the image intensity in that area has significant differences from other areas. Thus, the defect can be detected using a threshold segmentation method [15]. On the other hand, the defect area has large gradient variations in gray intensity, color and texture compared to the ideal reference surface area, thus the defect can be found by utilizing edge detection methods [16]. Moreover, as any difference from a product under test compared to the reference are regarded as defects, template matching techniques are frequently employed to detect defects [17]. However, the above methods all suffer from low reliability. This is because (a) threshold segmentation methods cannot be applied when the image intensity is distributed unevenly, (b) when a product has a complex surface, its own texture can greatly affect the reliability of edge detection, and (c) template matching requires preset segmentation thresholds; but image taken at different times can have large variation due to the influence of illumination that could cause detection errors. Since products having large-complex-surface possess problems from both uneven illumination and complex surface texture, therefore, traditional defect detection methods cannot be directly applied.

In order to detect defects of large-complex-surface products, a hybrid detection method combining gradient threshold segmentation and image registration is proposed. The source image is divided into two parts, namely, background and special pattern area. The background area has a small variation in its gray intensity and it can be seen as a continuous variation area. A gradient threshold segmentation method is used to detect the defects from the background. The gray intensity in the special pattern area with trademarks and characters has a larger variation, and a template matching method is employed to detect defects. Based on this, not only identification errors caused by uneven illumination can be avoided, but also the difficulty of detecting defect in product trademarks can be reduced. Furthermore, the proposed method has a wider prospect in engineering applications compared to existing methods.

The rest of this paper is organized as follows. Section II describes the characteristics of large-complex-surface images. In Section III, the proposed defect detection method is detailed. The experiment is presented in Section IV and results are also discussed. Finally, the conclusion is drawn in Section V.

II. IMAGE CHARACTERISTICS OF LARGE-COMPLEX-SURFACE

Figure 1 shows the surface image of an equipment cabinet and its gray intensity profile. The equipment cabinets were provided by EMERSON NETWORK POWER, and the surface images were captured using black-white smart cameras. The size of detection area on the equipment cabinet surface is 0.50m $\times$ 0.47m (width $\times$ height). Unlike the surface of simple steel sheets, this product has special patterns on its surface, it is difficult for traditional threshold segmentation methods to detect defects. Observing Fig. 1(b), the gray intensity profile map, the background has a significant difference in gray intensity to that of special patterns, especially on the edges of these two areas. Therefore, detection errors would arise when the special pattern edges are separated by edge detection algorithms.

Template matching methods are commonly used for defect detection of objects with complex surface [18]. However, as shown in Fig. 1(c), the background gray intensity profile is not constant due to the influence of factors such as uneven surface texture and uneven illumination, resulting in difficult image matching. Moreover, since the product has a large size, inappropriate placement can cause affine distortion including reflection, rotation, scaling and transformation in the product image, and produces errors in image registration. As aforementioned, threshold segmentation, edge detection and template matching cannot meet the strict requirements of defect detection for large-complex-surface. Hence, a hybrid method combining gradient threshold segmentation and image registration is developed.

III. THE PROPOSED METHOD

Figure 2 shows a flowchart of the proposed hybrid gradient threshold segmentation and image registration method. Firstly, surface images of products under test and the reference product are acquired and the images are divided into background area and special pattern area. For the background area, defect detection is conducted using the gradient threshold segmentation method. For the special pattern area, image registration and image difference techniques are used to identify defects. The principles of gradient threshold segmentation and image registration are explained in the following sections.

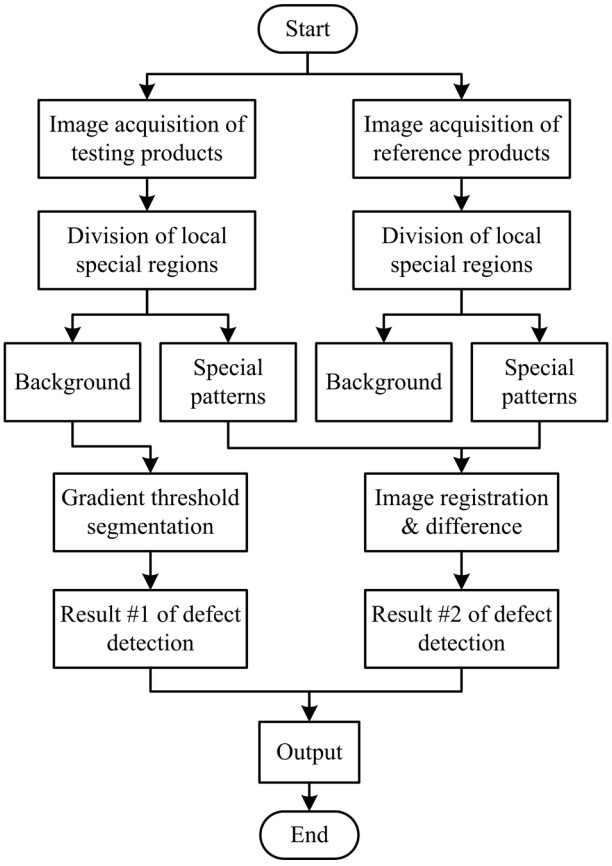

FIGURE 2. Flowchart of the large-complex-surface defect detection process.

A. GRADIENT THRESHOLD SEGMENTATION

When an image is acquired under uneven illumination (see Fig. 1), traditional threshold segmentation methods will fail to extract defect areas [19]. To solve the detecting problem caused by uneven illumination, by referring to the principle of edge detection, the gray gradient between defects and background can be used as an indicator for defect detection. In general, the gray gradient between two adjacent points can be expressed using two indicators: variation direction and variation magnitude. For a gray intensity image $f(x, y)$, the gradient vector $\nabla f(x, y)$ at point (x, y) can be expressed as

$$\nabla f(x,y) = \left[\frac{\partial f}{\partial x}, \frac{\partial f}{\partial y}\right]^{\top} = \begin{bmatrix} f_x(x,y) \\ f_y(x,y) \end{bmatrix} \tag{1}$$

where $f_x(x, y)$ and $f_y(x, y)$ are the variation rate of $f(x, y)$ on x-axis (horizontal) and on y-axis (vertical), respectively. Then the direction angle of $\nabla f(x, y)$ can be calculated as

$$\theta = \phi(x,y) = \arctan\left(\frac{f_y(x,y)}{f_x(x,y)}\right) \tag{2}$$

and the gradient amplitude $g(x, y)$ is

$$g(x,y) = \sqrt{f_x^2(x,y) + f_y^2(x,y)} \tag{3}$$

The gradient threshold segmentation method uses one or more threshold values to convert a gray intensity image into a binary image. The process can be mathematical expressed as

$$b(x,y) = \begin{cases} 1, & T_1 \le f(x,y) \le T_2 \\ 0, & \text{otherwise} \end{cases} \tag{4}$$

where $b(x, y)$ is the binary image, T_1 and T_2 are preset threshold values.

For rapid edge detection, differential operators can be used for fast and efficient detection. Roberts operator, Prewitt operator and Sobel operator are commonly used operators [20]. In particular, the Sobel operator incorporates direction differential operation with local weighted average. The weighted average of four adjacent pixel gray intensities is firstly calculated. Then the differences of gray intensity values are computed to suppress noises [21].

In general, metallic products are painted to prevent corrosion, and the texture of paint film will affect defect detection. Hence, the paint film texture is regarded as noises. Due to the fact that paint film belongs to the image background and its gray distribution is in the low-frequency domain, a high-pass frequency filter is applied to pre-process the metallic product surface image to reduce the influence of the paint film texture. To further suppress the influence of noise, the 3×3 Sobel operator is employed to obtain edge feature information [22]. Two convolution operators are used to represent the gradient vector of the image gray intensity. The horizontal and vertical direction convolution operators are

$$\begin{aligned} k_x(x,y) = {} & f(x-1,y+1) + 2f(x,y+1) + f(x+1,y+1) \\ & -f(x-1,y-1) - 2f(x,y-1) \\ & -f(x+1,y-1) \end{aligned} \tag{5}$$

$$\begin{aligned} k_y(x,y) = {} & f(x+1,y-1) + 2f(x+1,y) + f(x+1,y+1) \\ & -f(x-1,y-1) - 2f(x-1,y) \\ & -f(x-1,y+1) \end{aligned} \tag{6}$$

where $k_x(x, y)$ and $k_y(x, y)$ are the horizontal and vertical direction convolution kernel of the gray image $f(x, y)$, respectively.

Combining equations (4)–(6), the image gradient amplitude can be calculated. If $g(x, y) > T_3$ (T_3 is an appropriately

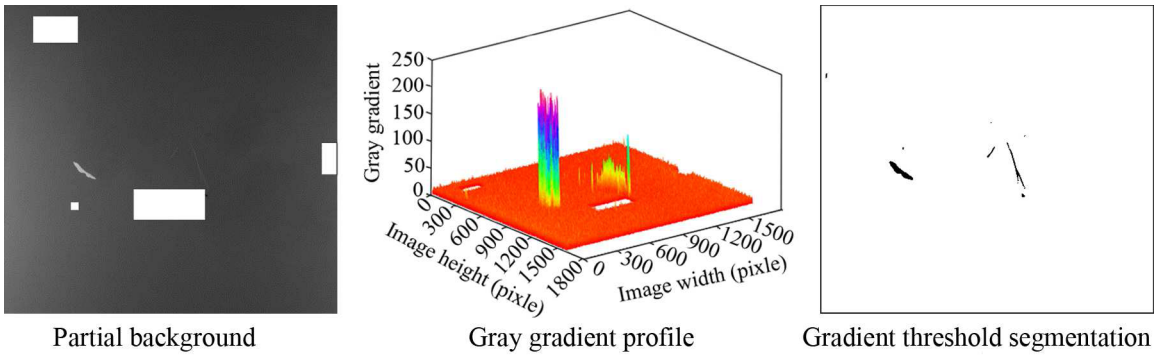

FIGURE 3. Defect detection of the background based on gradient threshold segmentation.

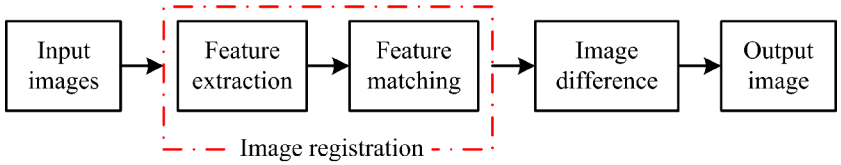

FIGURE 4. Flowchart of image registration and difference method.

selected threshold), then point (x, y) becomes the defect edge point. To ensure all the extracted points are on the edge of defects, threshold T_3 should be larger than the gradient caused by uneven illumination. In order to determine the T_3 value, a statistical analysis of the gray difference between defects and their background should be implemented. Fig. 3 shows an example of the gray gradient profile of a testing image. The statistical analysis is carried out using 100 example images and the result shows that the gray gradient value of the background is less than 20 pixels. Therefore, the segmentation threshold T_3 is set to 20 pixels. Based on this, the outcome of defect segmentation of Fig. 3(a) is shown in Fig. 3(c). It can be observed that the gradient threshold segmentation method provides higher robustness to uneven illumination and can effectively separate defects from varying backgrounds.

B. IMAGE REGISTRATION AND DIFFERENCING

Background difference [23] is usually adopted for rapid detection of surface defects in multiple local areas with complex patterns. In practice, because of inappropriate placement, the testing image and reference image may not be perfectly matched. Serious errors could occur after template differencing. Thus, image rectification has to be done before differencing is conducted, which matches the spatial position of the testing image to that of the reference image.

Image registration methods can be classified into two classes [24], [25]: gray-intensity-information based methods and feature based methods. Gray-intensity-information based methods are not suitable to process images with geometric deformations and radiometric discrepancies because of its strong dependence on gray intensity information [26]. Feature-based methods do not directly operate on image gray values, so it is insensitive to the variation of image gray intensity and object geometry shape. Therefore, a spatial transformation relationship is established by matching the significant features of the testing image and reference image. By doing so, image registration can be realized through testing image geometry rectification. A flowchart of the method is shown in Fig. 4. The input includes the testing image and the reference image. The feature information of the two images is extracted independently. Then image registration is performed by feature matching. Finally, the difference between the two images, after image registration, is obtained and used as an indicator in defect detection.

1) FEATURE EXTRACTION

Traditional feature-based image registration algorithms mainly integrate the speed-up robust features (SURF) algorithm and the scale-invariant feature transform (SIFT) algorithm for rapid feature extraction [27], [28]. To increase the computation speed and acquire higher accuracy in feature matching, Rublee in 2011 [29] proposed a fast algorithm based on the Features from Accelerated Segment Test (FAST) detector and the Binary Robust Independent Elementary Features (BRIEF) descriptor, called Oriented FAST and Rotated BRIEF (ORB). Compared to the SIFT and the SURF algorithm, the ORB algorithm is more suitable for online or real time feature detection. The ORB algorithm is composed of the oriented FAST (oFAST) feature detection and the rotated BRIEF (rBRIEF) feature description.

The principle of oFAST is that a feature point is firstly extracted using FAST and then is given a directional information to obtain rotational invariance. The main steps of the

oFAST are as below. More details about feature extraction program can be seen in references [29]–[32].

Step 1: rapid feature point extraction using the learned FAST algorithm [30].

Select a pixel point, p, with intensity $I(p)$. Denote a circle that traverses 16 pixels centered at the selected pixel location. When several consecutive pixels have intensity largely different from that of p, as well as the number of those pixels is greater than 9, point p is defined as a candidate angle point. The difference between pixel point strength should satisfy

$$|I(s) - I(p)| > \varepsilon \tag{7}$$

where $I(s)$ is the intensity of any pixel on the circle, ε is the preset threshold value that is application-dependent.

Step 2: angle points are screened with the Harris angle point response function, $R(A)$ [31].

To improve the accuracy of angle point detection, the angle point response function $R(A)$ in the Harris algorithm is introduced to filter the candidate angle points extracted in Step 1. The higher $R(A)$ values, the feature of a candidate point is more distinctive. $R(A)$ can be express as

$$R(A) = det(A) - \kappa \cdot trace^2(A) \tag{8}$$

where κ is a rectification factor with a range between 0.04 and 0.15, A is the Harris matrix [31]

$$A = 2\begin{bmatrix} \sum_{x_i \in W}\sum_{y_i \in W} X_i^2 & \sum_{x_i \in W}\sum_{y_i \in W} X_i Y_i \\ \sum_{x_i \in W}\sum_{y_i \in W} X_i Y_i & \sum_{x_i \in W}\sum_{y_i \in W} Y_i^2 \end{bmatrix} \tag{9}$$

where $X_i = \partial f(x_i, y_i)/\partial x$; $Y_i = \partial f(x_i, y_i)/\partial y$; x and y are the width and height of the testing image, respectively; W is the preset Harris angle point detection window. The window is centered at the candidate point p, and $W \in f(x, y)$.

After the $R(A)$ value of each angle point is computed, larger $R(A)$ at a certain ratio is selected to ensure the accuracy in angle point filtering. The selected ratio is application dependent and it is set at 60% in this work.

Step 3: search for the mass center of all angle points based on image moment computation [32].

The vector from an angle point to its adjacent mass center of gray intensity is used as the direction of the FAST angle point. The mass center of adjacent angle point gray intensity can be computed using image moment

$$m_{pq} = \sum_{x,y \in r} x_p y_q I(x, y) \tag{10}$$

where m_{pq} is the image $(p + q)$-order moment, and $p \in \mathbf{N}$, $q \in \mathbf{N}$; r is the radius of angle point adjacent area. Using image moment, the gray mass center C can be obtained from

$$C = \left(\frac{m_{10}}{m_{00}}, \frac{m_{01}}{m_{00}}\right) \tag{11}$$

Step 4: the vector formed by the angle point and the mass center is extracted as the angle point direction.

By utilizing the image moment, the direct angle θ of the angle point is

$$\theta = \arctan\left(\frac{m_{01}}{m_{10}}\right) \tag{12}$$

Besides direction information, a descriptor has to be added for angle point features. Select a series of pixel point-pairs in the adjacent area, assign binary values to those points which are determined on the basis of pixel intensities, that is,

$$\tau(p; x_i, y_i) = \begin{cases} 1, & P(x_i) < P(y_i) \\ 0, & \text{otherwise} \end{cases} \tag{13}$$

where $\tau(p; x_i, y_i)$ is the i-th point binary value, $P(x_i)$ and $P(y_i)$ are the pixel value of random points x_i and y_i in the adjacent area of the feature point p. Q pairs of point-pair (normally, $Q = 256$) are randomly selected from the window W, and a binary code is formed as

$$g_Q(p) = \sum_{1 \le t \le Q} 2^{t-1} \tau(p; x_i, y_i) \tag{14}$$

However, the binary code $g_Q(p)$ is non-rotation invariant, so it requires to be further processed. The matrix B is formed by the random selected Q pairs point-pair,

$$B = \begin{bmatrix} x_1, x_2, \ldots, x_Q \\ y_1, y_2, \ldots, y_Q \end{bmatrix} \tag{15}$$

The adjacent image-block of an angle point is rotated θ degrees calculated by equation (12), making the direction angle of the angle point to zero. The rotation matrix R_θ of the image-block is then obtained and the rotational matrix B_θ becomes

$$B_\theta = R_\theta B = \begin{bmatrix} [r]\cos\theta & -\sin\theta \\ \sin\theta & \cos\theta \end{bmatrix} B \tag{16}$$

Hence, equation (14) can be transformed to

$$g_Q(p, \theta) = g_Q(p) | (x_i, y_i) \in B_\theta \tag{17}$$

Compared to equation (14), the binary code shown in equation (17) is rotation invariant. Although the Q pairs of point-pair were selected randomly at first, after image rotation, the features of angle points become similar as relevance increases and distinctiveness decreases. Therefore, to increase the distinctiveness between each point-pair in the rotational image, a subset with better performance has to be selected from all candidate point-pairs. The best subset should have all feature points with an average of 0.5 and the minimum point-pair relevance.

2) FEATURE MATCHING

On the basis of ORB feature extraction, a 256-bit binary code is obtained for each feature point in the image. That is, every feature point is represented by a 256-dimension characteristic vector for ORB feature point matching. Hence, each feature point is assigned a specific position in this 256-dimension feature space. In order to look for the matching point of a feature point, the Hamming Distance in feature space between

the selected point and each candidate point are calculated. The Hamming Distance, D_H, is expressed as

$$D_H(x, y) = \sum C_{x_i} \oplus C_{y_i} \tag{18}$$

where, C_{x_i} and C_{y_i} are the i-th code of the two feature vectors; $\oplus$ represents the exclusive or operation. A smaller D_H value means a higher degree of matching. Thus, the point with the minimum D_H is the matched point.

The feature matching result is used to find the spatial transformation relationship and mapping function between the testing image and the template image to facilitate the registration of two images. The mapping function can be represented by a homograph matrix. For a two-dimensional image, the homograph matrix H can be represented by a homo-order three-dimensional vector [20]

$$H = \begin{bmatrix} h_{11} & h_{12} & h_{13} \\ h_{21} & h_{22} & h_{23} \\ h_{31} & h_{32} & h_{33} \end{bmatrix} \tag{19}$$

Then, the linear transformation relationship between every feature point-pair is

$$\begin{bmatrix} x' \\ y' \\ 1 \end{bmatrix} = \begin{bmatrix} h_{11} & h_{12} & h_{13} \\ h_{21} & h_{22} & h_{23} \\ h_{31} & h_{32} & h_{33} \end{bmatrix} \begin{bmatrix} x \\ y \\ 1 \end{bmatrix} \tag{20}$$

Equation (20) can be converted into

$$\begin{cases} h_{11}x + h_{12}y + h_{13} - h_{31}xx' - h_{32}yx' - h_{33}x' = 0 \\ h_{21}x + h_{22}y + h_{23} - h_{31}xy' - h_{32}yy' - h_{33}y' = 0 \end{cases} \tag{21}$$

Select n ($n \geq 4$) matching feature point-pairs, (x_1, y_1) and (x'_1, y'_1), (x_2, y_2) and (x'_2, y'_2), $\cdots$, (x_n, y_n) and (x'_n, y'_n), and a matrix equation is obtained as

$$Fh = [0, 0, \cdots, 0]^T_{1\times 9} \tag{22}$$

where

$$F = \begin{bmatrix} x_1 & y_1 & 1 & 0 & 0 & 0 & -x_1x'_1 & -y_1x'_1 & -x'_1 \\ 0 & 0 & 0 & x_1 & y_1 & 1 & -x_1y'_1 & -y_1y'_1 & -y'_1 \\ x_2 & y_2 & 1 & 0 & 0 & 0 & -x_2x'_2 & -y_2x'_2 & -x'_2 \\ 0 & 0 & 0 & x_2 & y_2 & 1 & -x_2y'_2 & -y_2y'_2 & -y'_2 \\ \vdots & \vdots & \vdots & \vdots & \vdots & \vdots & \vdots & \vdots & \vdots \\ x_n & y_n & 1 & 0 & 0 & 0 & -x_nx'_n & -y_nx'_n & -x'_n \\ 0 & 0 & 0 & x_n & y_n & 1 & -x_ny'_n & -y_ny'_n & -y'_n \end{bmatrix} \tag{23}$$

$$h = [h_{11}, h_{12}, h_{13}, h_{21}, h_{22}, h_{23}, h_{31}, h_{32}, h_{33}]^T \tag{24}$$

Equation (22) does not have a deterministic solution, so singular value decomposition is used to acquire the minimum least squares solution. However, if false matching points exist among the selected points, errors in transformation relationship would result, leading to the failure of image transformation. To deal with this problem, the random sample consensus (RANSAC) algorithm [33] is applied to calculate statistical parameters of sampling feature points. The principle of the RANSAC algorithm is explained in the following.

Four point-pairs are first randomly selected from all feature points (the homograph matrix can be calculated with at least four point-pairs). The homograph matrix is then calculated from equation (22). Whereas, the homograph matrix H needs to be verified using other matching points. For example, for matching feature points (x_i, y_i) and (x'_i, y'_i), the angle point coordinate (x_i, y_i) of the testing image has a homo-order expression $[x_i, y_i, 1]^\top$. The homo-order expression $[\hat{x}_i, \hat{y}_i, 1]^\top$ of the mapping point $(\hat{x}_i, \hat{y}_i)$ can be found using equation (20), we have

$$\begin{bmatrix} \hat{x}_i \\ \hat{y}_i \\ 1 \end{bmatrix} = H \begin{bmatrix} x_i \\ y_i \\ 1 \end{bmatrix} \tag{25}$$

If the location difference between $(\hat{x}_i, \hat{y}_i)$ and (x'_i, y'_i) is smaller than preset threshold value η (normally, $\eta = 3$) [34], that is

$$\sqrt{(\hat{x}_i - x'_i)^2 + (\hat{y}_i - y'_i)^2} < \eta \tag{26}$$

then the matching feature point-pair (x_i, y_i) and (x'_i, y'_i) is considered satisfying the homograph matrix model. Due to the fact that the sampling of point-pair is random and the homograph matrix is generated from each sample, the more point-pairs that satisfy equation (26), the higher the confidence level. Thus, the more recursive sampling, the higher probability is achieved in finding a suitable homograph matrix. Considering program executive efficiency, the maximum number of recursive sampling is here set to 2000. Meanwhile, the homograph matrix with the highest confidence level is selected as the spatial transformation model between the template and testing images, as shown in Fig. 5(a) and Fig. 5(b). It can be observed that skew occurred in the testing image because of mis-placement. The testing image is converted by feature mapping based on the spatial transformation relationship and the result is shown in Fig. 5(c). It shows that the testing image after registration has significantly smaller difference in position bias to the reference image. This is helpful to ensure that the proposed method is suitable to solve the geometric deformations problems caused by environmental factors and can be robustly applied.

3) IMAGE DIFFERENCING

The image difference method is applied for defect detection after image registration. Assume the reference image is $T(x, y)$ and the testing image is $S(x, y)$, and their difference image is

$$D(x, y) = |T(x, y) - S(x, y)| \tag{27}$$

If there are no defects, all pixels in the difference image should all be zero. In practices, the gray intensity profile of surface images captured in different times could be different because of varying surface roughness, uneven illumination and environmental factors. Therefore, a threshold T_4 has to be set to binarize the difference image, and the binary

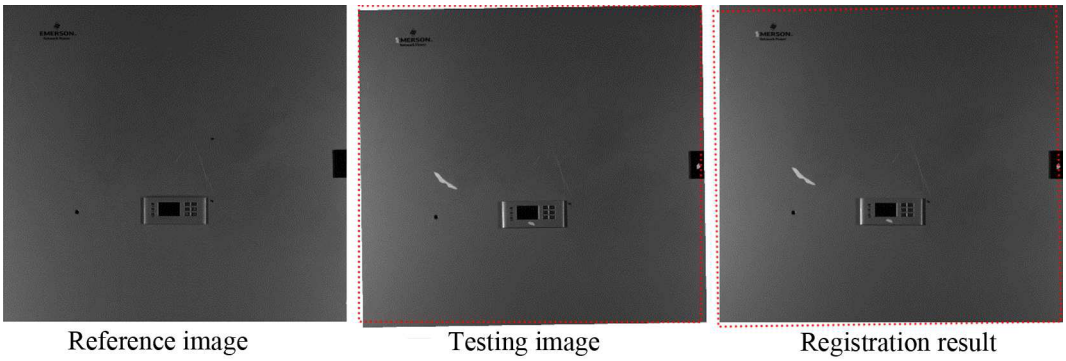

FIGURE 5. Testing image with spatial transformation and its registration result.

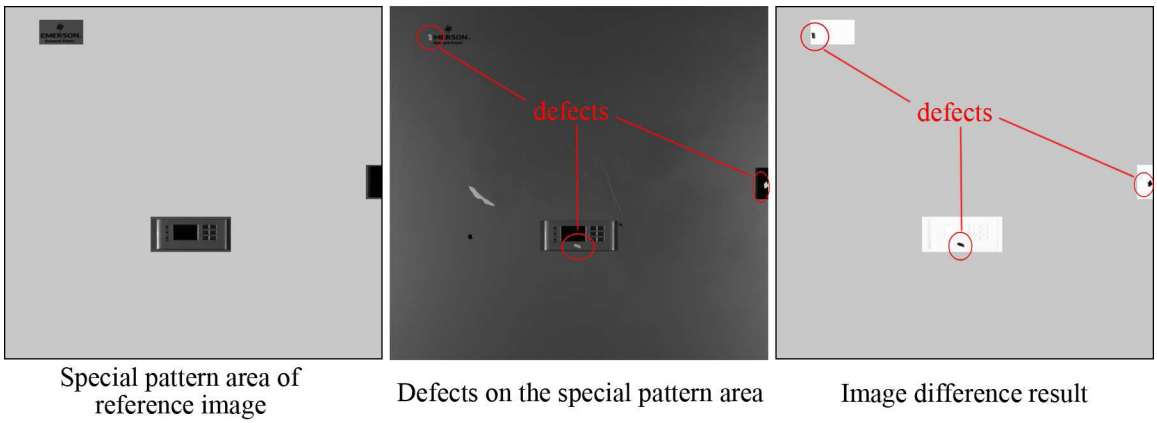

FIGURE 6. Defect detection result for special pattern area based on image registration and image difference method.

image $B(x, y)$ is expressed as

$$B(x,y) = \begin{cases} 1, & D(x,y) > T_4 \\ 0, & \text{otherwise} \end{cases} \tag{28}$$

Threshold T_4 can be obtained by adaptive calculation using the Otsu algorithm [35]. Considering various illumination conditions and defect types, the improved Otsu method proposed by Yuan *et al.* [12] was employed to acquire T_4. This method was proved to be more suitable to detect various defects as compared with the valley-emphasis and the neighborhood valley-emphasis methods.

After image registration, as discussed in Section III-B.2, image segmentation is conducted using image difference and the result is shown in Fig. 6. It can be found that defects in the special pattern area are effectively detected, and the defect detection problem for special pattern surfaces is solved by combining image registration and image difference methods. Finally, the whole image defect detection result is obtained by integrating results shown in Fig. 3(b) and Fig. 6(c).

IV. EXPERIMENT AND DISCUSSION

The performance of the proposed hybrid method and traditional methods of threshold segmentation and background difference are compared. It is worth to point out that, with fixed working condition and camera installation, images taken from the same product that contains large-complex-surfaces during automatic production should remain the same except for the difference caused by illumination variation, object orientation and surface defects, as shown in Fig. 7. The size of the detecting area in equipment cabinet surface, shown in Fig. 7(a), is 0.50m $\times$ 0.47m and the image resolution is 1750 $\times$ 1645 pixels. The coordinates shown in the figure are the screw hole center. The variation of coordinate values shows the shift of feature location. Fig. 7(a) is the reference image of an ideal product, with the screw hole center coordinate of (376, 1109). Shift occurs in Fig. 7(g) and Fig. 7(h), and the coordinates are (461, 1113) and (370, 1116), respectively.

It can be seen that the brightness of all images are different. Let the illumination intensity of the reference image be the 'normal illumination' condition. Thus, the illumination in Fig. 7(c) is 'brighter', in Fig. 7(d) is 'darker', in Fig. 7(e) is 'left-bright & right-dark' and in Fig. 7(f) is 'left-dark & right-bright.' To clearly illustrate the difference of illumination intensity and illumination distribution in Fig. 7, images are converted into gray intensity maps, as shown in Fig. 8. It can be clearly seen that images captured at different periods have difference illumination intensity. Especially, even if taken

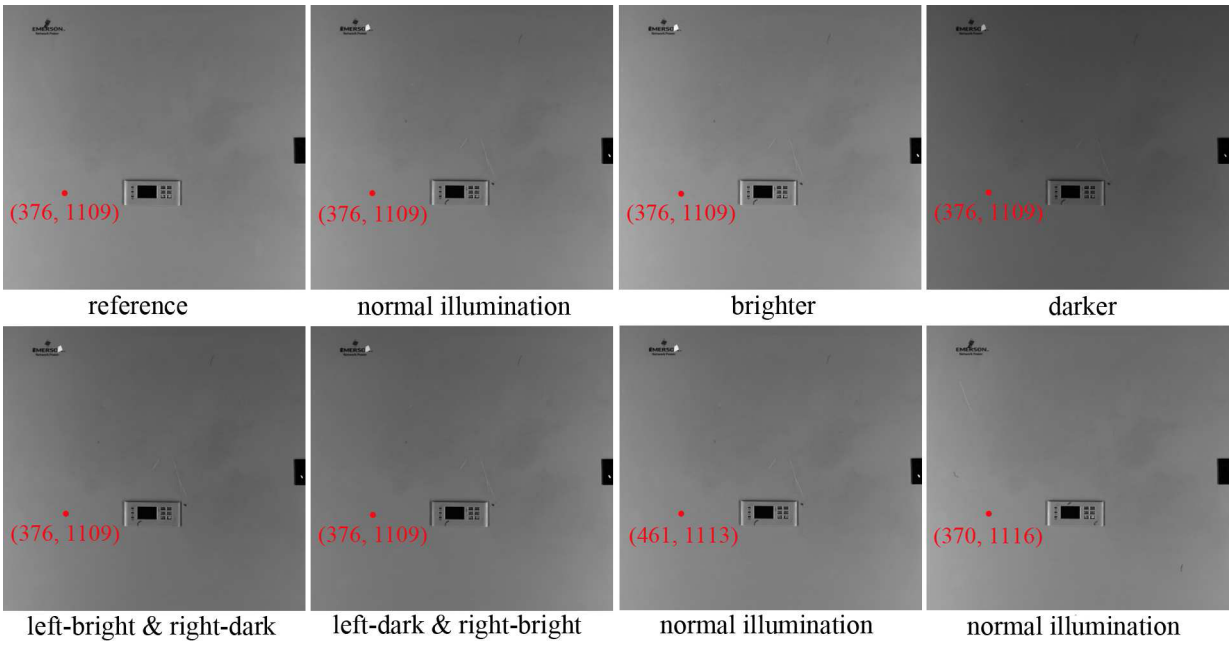

FIGURE 7. Images of equipment cabinet taken under different conditions.

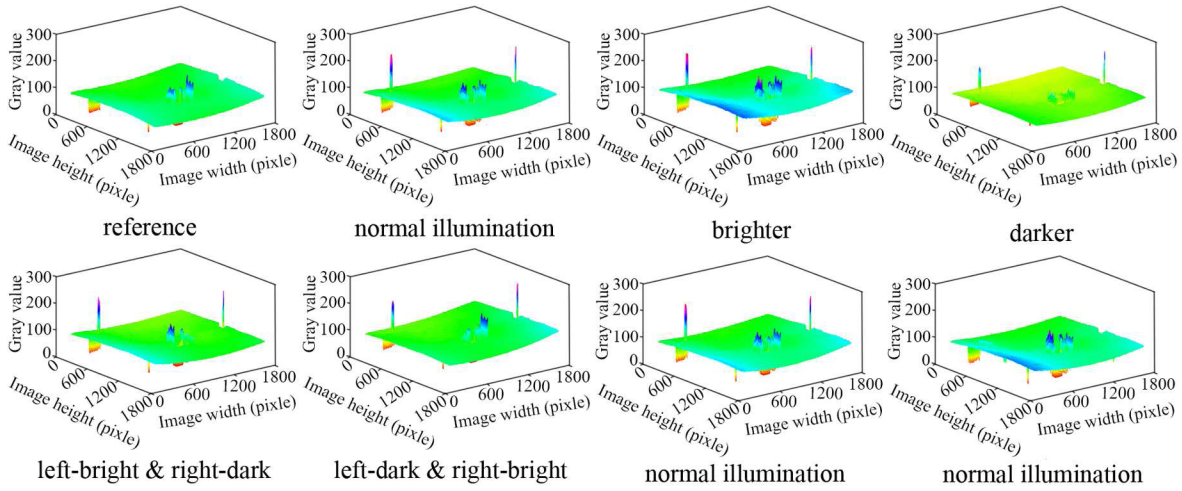

FIGURE 8. Gray intensity profile maps corresponding to the subplots in Fig. 7.

under the 'normal illumination' condition, the overall gray intensity profile of the shifted product is still different from the reference image.

Defect detection results from the gradient threshold segmentation method (GTS), the template matching method (TM) and the gradient threshold segmentation and image registration method (GTS-IR), on images depicted in Fig. 7, are shown in Fig. 9, 10 and 11 respectively. In Fig. 9, it can be found that GTS can locate the area where edge gradient changes significantly. Because of this, the special patterns are also mis-detected as defects due to the fact that their gray intensities are much different from that of the background. In contrast, defects cannot be identified when their gray intensities are close to that of the background.

It can be observed from Fig. 10 that the difference between the testing and reference images results in defect detection failures. Some of the local background areas in Fig. 10(d) and (f) are mis-judged as defects. Fig. 10(g) and (h) shows that, when the equipment cabinet has positional shift, matching errors of local pattern areas are caused only using TM without image registration, and some of the pattern edges are mis-judged as defects.

Figure 11 shows the detection results of the GTS-IR process. It can be observed that GTS-IR can realize defect detection for the whole image. Defect detection in the

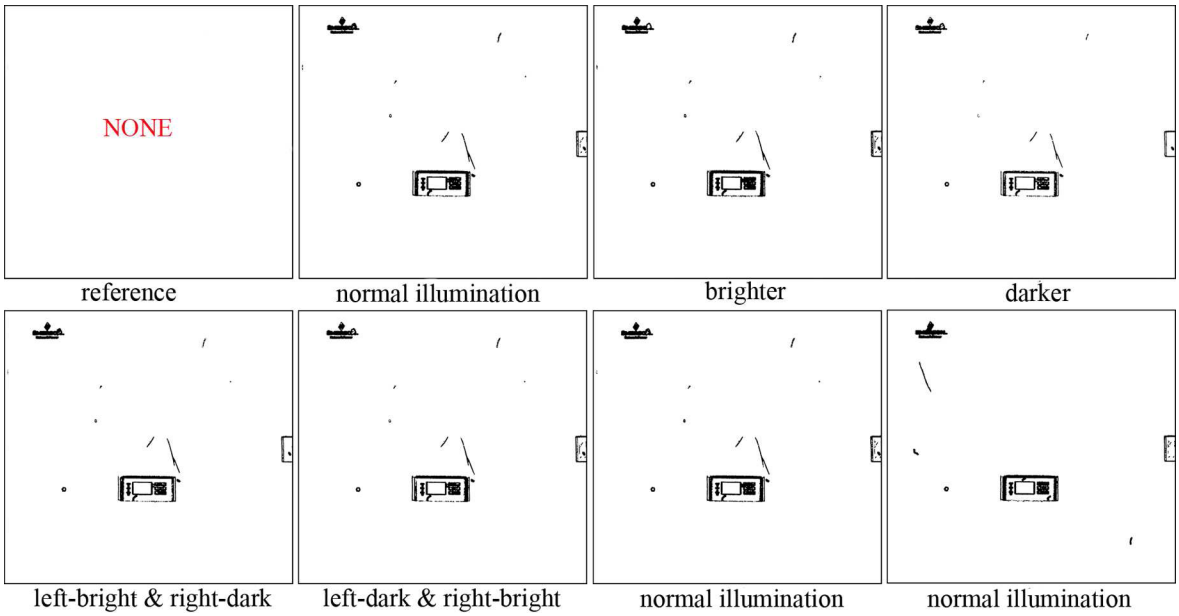

FIGURE 9. Defect detection results of Fig. 7 using the GTS.

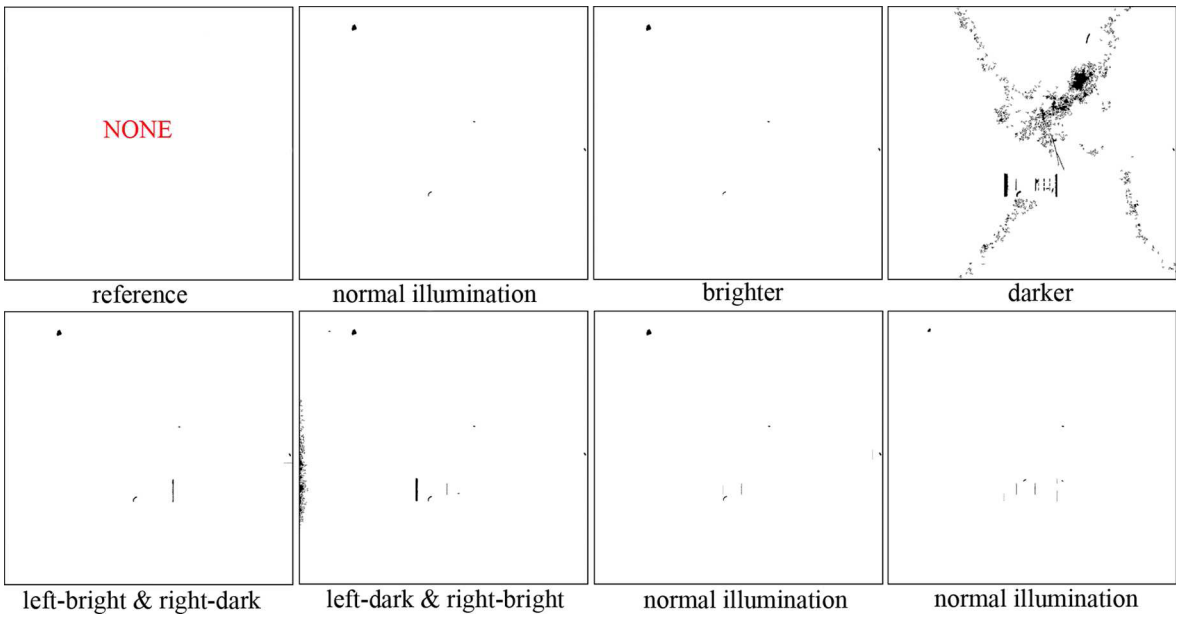

FIGURE 10. Defect detection results of Fig. 7 using the TM.

background maintains good accuracy even with illumination intensity variation. However, a few detection errors still occur in special pattern areas, as shown in Fig. 11(d) and (f).

This is because the special pattern area has complex texture, and the illumination variation significantly impacts the texture brightness and image registration only rectifies the feature position error but cannot compensate for the effect of uneven illumination, which may cause matching errors. Despite of this, higher detection accuracy of special patterns by combining image registration is acquired compared to that of directly using TM as shown in Fig. 10.

For further evaluation, a quantitative analysis is performed. The purpose of the proposed hybrid method is to improve the accuracy of defect detection, and thus the indicators of *Precision*, *Recall* and *F-measure* are employed to evaluate the performance of GTS, TM and GTS-IR, which are expressed by [36]

$$Precision = \frac{TP}{TP + FP} \tag{29}$$

$$Recall = \frac{TP}{TP + FN} \tag{30}$$

$$F\text{-}measure = \frac{2 \times Precision \times Recall}{Precision + Recall} \tag{31}$$

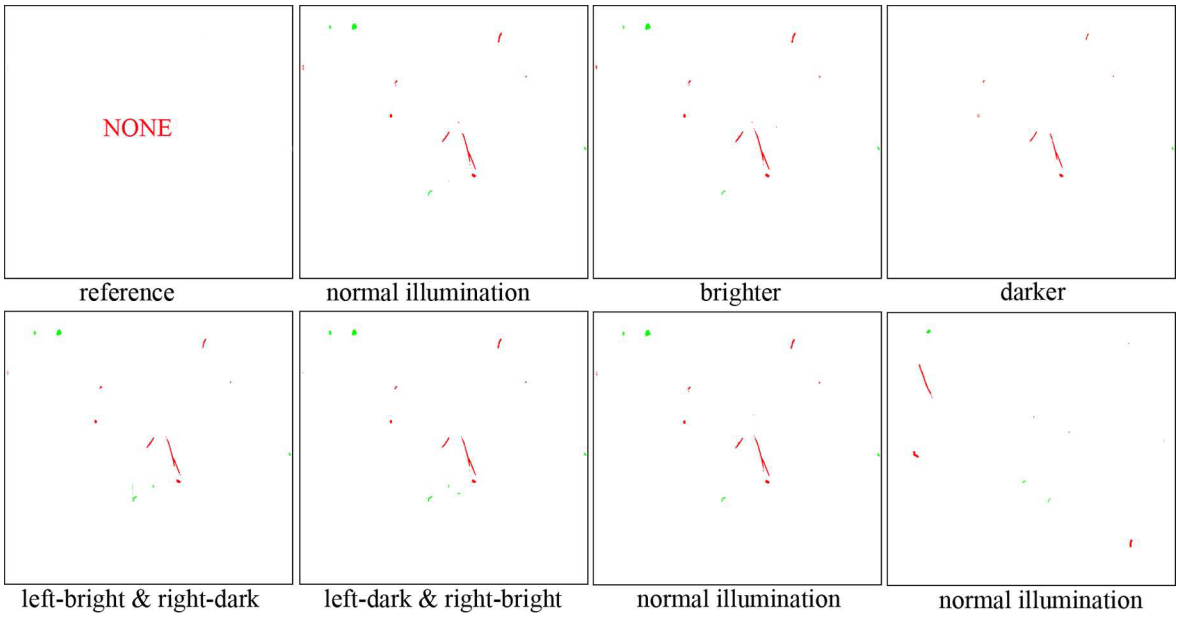

FIGURE 11. Defect detection results of Fig. 7 using the GTS-IR.

TABLE 1. Detection performance of different algorithms on the equipment cabinet images in Fig. 7.

Image		Fig. 7(b)	Fig. 7(c)	Fig. 7(d)	Fig. 7(e)	Fig. 7(f)	Fig. 7(g)	Fig. 7(h)
GTS	*TP*	8	8	7	8	7	8	3
	FP	4	4	4	4	4	4	4
	FN	4	4	5	4	5	4	5
	Precision	0.67	0.67	0.64	0.67	0.64	0.67	0.43
	Recall	0.67	0.67	0.58	0.67	0.58	0.67	0.38
	F-measure	0.67	0.67	0.61	0.67	0.61	0.67	0.40
TM	*TP*	4	4	2	4	6	4	4
	FP	0	0	126	2	3	3	4
	FN	9	9	11	9	8	9	4
	Precision	1.00	1.00	0.02	0.67	0.67	0.57	0.50
	Recall	0.31	0.31	0.46	0.31	0.43	0.31	0.50
	F-measure	0.47	0.47	0.03	0.42	0.52	0.40	0.50
GTS-IR	*TP*	12	12	8	13	13	12	8
	FP	0	1	0	1	1	0	1
	FN	1	1	5	0	0	1	0
	Precision	1.00	0.92	1.00	0.93	0.93	1.00	0.89
	Recall	0.92	0.92	0.62	1.00	1.00	0.92	1.00
	F-measure	0.96	0.92	0.76	0.96	0.96	0.96	0.94

where *TP* is the number of correctly detected defects; *FP* is the number of non-defects that are mis-judged as defects; *FN* is the number of defects that are mis-judged as non-defects. The above accuracy parameters of equipment cabinet in Fig. 7 detected by GTS, TM and GTS-IR are shown in TABLE 1.

As can be seen in TABLE 1, the *Precision*, *Recall* and *F-measure* of GTS-IR are respectively in range of [0.89, 1.00], [0.62, 1.00] and [0.76, 0.96], which are all larger than that of GTS and TM correspondingly. Although the *Precision* of TM can reach 1.00, which is higher than that of GTS, it can be found that the *Precision* and *F-measure* obtained from the test case shown in Fig. 7(d) are only 0.02 and 0.03. This is because some background areas are mis-detected as defects, and *FP* reaches 126 that is much larger than the real defect number of 13. These results clearly demonstrate that the proposed method, GTS-IR, is able to achieve higher accuracy in large-complex-surface defect detection.

In the experiment, 100 equipment cabinet images were captured and tested. Fig. 12 shows the box-plot of *Precision*, *Recall* and *F-measure* acquired from the processed testing images using the method of GTS, TM and GTS-IR. The mean *Precision*, *Recall* and *F-measure* values of GTS-IR (0.90, 0.93 and 0.91) are the highest, and the *F-measure* is about 1.21 times and 2.94 times higher than that of GTS and TM respectively. This result indicates that the proposed hybrid algorithm is superior in detecting defects on large complex surfaces by separating the image to background and spatial pattern areas.

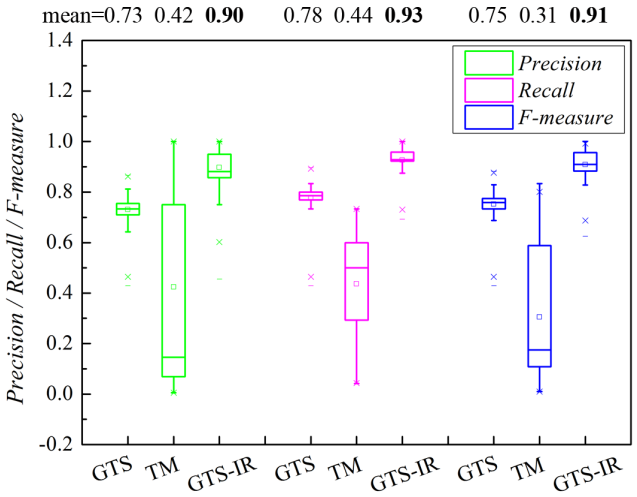

FIGURE 12. The box-plot of Precision, Recall and F-measure obtained from 100 testing images processed using GTS, TM and GTS-IR respectively.

To sum up, the proposed hybrid algorithm achieves improvement in defect detection accuracy as compared to traditional defect detection methods and is more suitable for large-complex-surface defect detection. In spite of this, it still needs to be mentioned that the proposed hybrid method, containing gradient threshold segmentation, image registration and image difference algorithms, is more complicate and takes longer execution times than tradition methods. Correspondingly, further improvements need to be done regarding the efficiency, robustness against illumination variation and the self-adaption of image registration. In future work, image enhancement algorithms will be applied to improve the image quality in areas where the defect has low-contrast against the background, which is helpful to reduce the influence of illumination variation. Moreover, the image registration algorithm will be optimized to deal with problems concerning image distortion and significant shift. This will be helpful to promote the application of visual detection techniques in industry regarding defect detection.

V. CONCLUSION

To meet the requirements of vision-based quality inspection for large size and complex surfaces, a hybrid method combining gradient threshold segmentation and image registration for defect detection is developed. The main conclusions that can be identified from experimental results include:

- The gradient threshold segmentation method can be used to detect defects based on the significant gray difference between defects and the background. Mis-detection errors caused by the special pattern area can be effectively reduced, and the *F-measure* of 0.75 is much higher than that obtained by template matching method (0.31), which demonstrates that gradient threshold segmentation is robust to illumination variation on large-scale surfaces.
- Compared to traditional gradient threshold segmentation and template matching methods, the proposed method that integrates image registration and image difference to detect defects on complex patterns under image distortion and image shift, has demonstrated a higher accuracy (*Precision* of 0.90, *Recall* of 0.93 and *F-measure* of 0.91).
- Future work needs to reduce the illumination influence on a large surface. To this end, the image quality could be further improved by enhancing the contrast between defects and their background. Meanwhile, the defect detection method should be optimized to adaptively acquire segmentation thresholds.

REFERENCES

[1] M. H. Karimi and D. Asemani, "Surface defect detection in tiling industries using digital image processing methods: Analysis and evaluation," *ISA Trans.*, vol. 53, no. 3, pp. 834–844, 2014.
[2] C. Koch, K. Georgieva, V. Kasireddy, B. Akinci, and P. Fieguth, "A review on computer vision based defect detection and condition assessment of concrete and asphalt civil infrastructure," *Adv. Eng. Inform.*, vol. 29, no. 2, pp. 196–210, 2015.
[3] B. Zhang *et al.*, "Computer vision detection of defective apples using automatic lightness correction and weighted RVM classifier," *J. Food Eng.*, vol. 146, pp. 143–151, Feb. 2015.
[4] B. Zhang *et al.*, "Principles, developments and applications of computer vision for external quality inspection of fruits and vegetables: A review," *Food Res. Int.*, vol. 62, pp. 326–343, Aug. 2014.
[5] C. Jian, J. Gao, and Y. Ao, "Automatic surface defect detection for mobile phone screen glass based on machine vision," *Appl. Soft Comput.*, vol. 52, pp. 348–358, Mar. 2017.
[6] R. C. Tighe, J. Dulieu-Barton, and S. Quinn, "Identification of kissing defects in adhesive bonds using infrared thermography," *Int. J. Adhes. Adhesives*, vol. 64, pp. 168–178, Oct. 2015.
[7] K. Yildiz, A. Buldu, M. Demetgul, and Z. Yildiz, "A novel thermal-based fabric defect detection technique," *J. Textile Inst.*, vol. 106, no. 3, pp. 275–283, 2015.
[8] K. Yıldız and A. B. M. Demetgul, "A thermal-based defect classification method in textile fabrics with K-nearest neighbor algorithm," *J. Ind. Textiles*, vol. 45, no. 5, pp. 780–795, 2014.
[9] N. Kotwaliwale, K. Singh, A. Kalne, S. N. Jha, N. Seth, and A. Kar, "X-ray imaging methods for internal quality evaluation of agricultural produce," *J. Food Sci. Technol.*, vol. 51, no. 1, pp. 1–15, 2014.
[10] K. Liu, H. Wang, H. Chen, E. Qu, Y. Tian, and H. Sun, "Steel surface defect detection using a new Haar–Weibull-variance model in unsupervised manner," *IEEE Trans. Instrum. Meas.*, vol. 66, no. 10, pp. 2585–2596, Oct. 2017.
[11] C.-L. Tien, Q.-H. Lai, and C.-S. Lin, "Development of optical automatic positioning and wafer defect detection system," *Meas. Sci. Technol.*, vol. 27, no. 2, p. 025205, 2016.
[12] X.-C. Yuan, L.-S. Wu, and Q. Peng, "An improved Otsu method using the weighted object variance for defect detection," *Appl. Surf. Sci.*, vol. 349, pp. 472–484, Sep. 2015.
[13] Y. Zhang, T. Li, and Q. Li, "Defect detection for tire laser shearography image using curvelet transform based edge detector," *Opt. Laser Technol.*, vol. 47, pp. 64–71, Apr. 2013.
[14] X. Bai, Y. Fang, W. Lin, L. Wang, and B.-F. Ju, "Saliency-based defect detection in industrial images by using phase spectrum," *IEEE Trans. Ind. Inform.*, vol. 10, no. 4, pp. 2135–2145, Nov. 2014.
[15] X. Li, H. Jiang, and G. Yin, "Detection of surface crack defects on ferrite magnetic tile," *NDT E Int.*, vol. 62, pp. 6–13, Mar. 2014.
[16] Z. Hocenski, S. Vasilic, and V. Hocenski, "Improved Canny edge detector in ceramic tiles defect detection," in *Proc. 32nd Annu. Conf. IEEE Ind. Electron.*, Paris, France, Nov. 2006, pp. 3328–3331.
[17] J. Kim, "Template-based defect detection of a brazed heat exchanger using an X-ray image," *Opt. Eng.*, vol. 52, no. 3, p. 036501, 2013.

[18] C.-C. Wang, B. C. Jiang, J.-Y. Lin, and C.-C. Chu, "Machine vision-based defect detection in IC images using the partial information correlation coefficient," *IEEE Trans. Semicond. Manuf.*, vol. 26, no. 3, pp. 378–384, Aug. 2013.
[19] M. H. Karimi and D. Asemani, "A novel histogram thresholding method for surface defect detection," in *Proc. 8th Iranian Conf. Mach. Vis. Image Process.*, Zanjan, Iran, Sep. 2013, pp. 95–99.
[20] M. Sonka, V. Hlavac, and R. Boyle, *Image Processing, Analysis, and Machine Vision*, 4th ed. Boston, MA, USA: Cengage, 2013.
[21] A. M. Al-Ghaili, S. Mashohor, A. R. Ramli, and A. Ismail, "Vertical-edge-based car-license-plate detection method," *IEEE Trans. Veh. Technol.*, vol. 62, no. 1, pp. 26–38, Jan. 2013.
[22] C. I. Gonzalez, P. Melin, J. R. Castro, O. Mendoza, and O. Castillo, "An improved sobel edge detection method based on generalized type-2 fuzzy logic," *Soft Comput.*, vol. 20, no. 2, pp. 773–784, Feb. 2016.
[23] Y. Peng, T. Wu, S. Wang, and Z. Peng, "Oxidation wear monitoring based on the color extraction of on-line wear debris," *Wear*, vols. 332–333, pp. 1151–1157, May/Jun. 2015.
[24] B. Zitová and J. Flusser, "Image registration methods: A survey," *Image Vis. Comput.*, vol. 21, pp. 977–1000, Oct. 2003.
[25] F. P. M. Oliveira and J. M. R. S. Tavares, "Medical image registration: A review," *Comput. Methods Biomech. Biomed. Eng.*, vol. 17, no. 2, pp. 73–93, 2014.
[26] M. Gong, S. Zhao, L. Jiao, D. Tian, and S. Wang, "A novel coarse-to-fine scheme for automatic image registration based on SIFT and mutual information," *IEEE Trans. Geosci. Remote Sens.*, vol. 52, no. 7, pp. 4328–4338, Jul. 2014.
[27] D. G. Lowe, "Distinctive image features from scale-invariant keypoints," *Int. J. Comput. Vis.*, vol. 60, no. 2, pp. 91–110, 2004.
[28] H. Bay, T. Tuytelaars, and L. Van Gool, "SURF: Speeded up robust features," in *Proc. Eur. Conf. Comput. Vis.*, Graz, Austria, 2006, pp. 404–417.
[29] E. Rublee, V. Rabaud, K. Konolige, and G. Bradski, "ORB: An efficient alternative to SIFT or SURF," in *Proc. IEEE Int. Conf. Comput. Vis.*, Barcelona, Spain, Nov. 2011, pp. 2564–2571.
[30] E. Rosten and T. Drummond, "Machine learning for high-speed corner detection," in *Proc. 9th Eur. Conf. Comput. Vis.*, Graz, Austria, 2006, pp. 403–443.
[31] F. Bellavia, D. Tegolo, and C. Valenti, "Improving Harris corner selection strategy," *IET Comput. Vis.*, vol. 5, no. 2, pp. 87–96, Mar. 2011.
[32] E. G. Karakasis, A. Amanatiadis, A. Gasteratos, and S. A. Chatzichristofis, "Image moment invariants as local features for content based image retrieval using the bag-of-visual-words model," *Pattern Recognit. Lett.*, vol. 55, pp. 22–27, Apr. 2015.
[33] R. Hartley and A. Zisserman, *Multiple View Geometry in Computer Vision*, 2nd ed. Cambridge, U.K.: Cambridge Univ. Press, 2003.
[34] L. R. Dung, C. M. Huang, and Y. Y. Wu, "Implementation of RANSAC algorithm for feature-based image registration," *J. Comput. Commun.*, vol. 1, pp. 46–50, Nov. 2013.
[35] Y. Peng, T. Wu, S. Wang, N. Kwok, and Z. Peng, "Motion-blurred particle image restoration for on-line wear monitoring," *Sensors*, vol. 15, no. 4, pp. 8173–8191, 2015.
[36] S. Ghorai, A. Mukherjee, M. Gangadaran, and P. K. Dutta, "Automatic defect detection on hot-rolled flat steel products," *IEEE Trans. Instrum. Meas.*, vol. 62, no. 3, pp. 612–621, Mar. 2013.

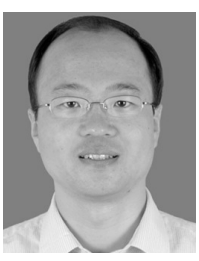

GUANGZHONG CAO received the B.Sc., M.Sc., and Ph.D. degrees in electrical engineering and automation from Xi'an Jiaotong University, China, in 1989, 1992, and 1996, respectively. He is currently a Professor and the Director of the Shenzhen Key Laboratory of Electromagnetic Control, Shenzhen University, China. He has authored over 80 articles published in refereed journals and conference proceedings. His research interests include control theory, robotic technology, machine vision, and information processing.

SONGBO RUAN received the B.Sc. degree in intelligence science and technology from South Central University for Nationalities, China, in 2016. He is currently pursuing the master's degree in control science and engineering with the Shenzhen Key Laboratory of Electromagnetic Control, Shenzhen University, China. His research interests include machine vision and information processing.

YEPING PENG received the B.Sc. degree in mechanical design, manufacture, and automation from Harbin Engineering University, China, in 2011, and the M.Sc. and Ph.D. degrees in mechanical engineering from Xi'an Jiaotong University, China, in 2014 and 2017, respectively. She is currently an Assistant Professor with the Shenzhen Key Laboratory of Electromagnetic Control, College of Mechatronics and Control Engineering, Shenzhen University, China. Her main research interests include machine vision, image processing, and signal processing.

SUDAN HUANG received the B.Sc. and M.Sc. degrees in control theory and control engineering from Shenzhen University, China, in 2009 and 2012, respectively, and the Ph.D. degree in electrical engineering from Southwest Jiaotong University, China. She is currently an Assistant Professor with the Shenzhen Key Laboratory of Electromagnetic Control, College of Mechatronics and Control Engineering, Shenzhen University. Her research interests include information processing, control theory, and its applications.

NGAIMING KWOK received the B.Sc. degree in computer science from the University of East Asia, Macau, the M.Sc. degree in control engineering from The Hong Kong Polytechnic University, Hong Kong, and the Ph.D. degree in mobile robotics from the University of Technology, Sydney, Australia, in 1993, 1997, and 2007 respectively. He is currently a Lecturer with the School of Mechanical and Manufacturing Engineering, University of New South Wales, Sydney. He has published over 150 journal articles and conference papers. His research interests include intelligent computation, image processing, and automatic control.